sensors

MDPI

*Article*

# ZnO/$MO_x$ Nanofiber Heterostructures: $MO_x$ Receptor's Role in Gas Detection

**Vadim Platonov [1], Oleg Sinyashin [2] and Marina Rumyantseva [1,*]**

[1] Chemistry Department, Moscow State University, Moscow 119991, Russia
[2] Federal Research Center Kazan Scientific Center RAS, Kazan 420111, Russia
* Correspondence: roum@inorg.chem.msu.ru; Tel.: +7-495-939-5471

**Abstract:** ZnO/$MO_x$ (M = $Fe^{III}$, $Co^{II,III}$, $Ni^{II}$, $Sn^{IV}$, $In^{III}$, $Ga^{III}$; [M]/([Zn] + [M]) = 15 mol%) nanofiber heterostructures were obtained by co-electrospinning and characterized by X-ray diffraction, scanning electron microscopy and X-ray fluorescence spectroscopy. The sensor properties of ZnO and ZnO/$MO_x$ nanofibers were studied toward reducing gases CO (20 ppm), methanol (20 ppm), acetone (20 ppm), and oxidizing gas $NO_2$ (1 ppm) in dry air. It was demonstrated that the temperature of the maximum sensor response of ZnO/$MO_x$ nanofibers toward reducing gases is primarily influenced by the binding energy of chemisorbed oxygen with the surface of the modifier's oxides. When detecting oxidizing gas $NO_2$, high sensitivity at a low measurement temperature can be achieved with a high concentration of free electrons in the near-surface layer of zinc oxide grains, which is determined by the band bending at the ZnO/$MO_x$ interface characterized by the difference in the electron work function of ZnO and $MO_x$.

**Keywords:** ZnO nanofibers; surface modification; binding energy of chemisorbed oxygen; heterojunction; band bending; semiconductor gas sensor



Academic Editor: Michele Penza

Received: 6 December 2024
Revised: 31 December 2024
Accepted: 8 January 2025
Published: 10 January 2025

**Citation:** Platonov, V.; Sinyashin, O.; Rumyantseva, M. ZnO/$MO_x$ Nanofiber Heterostructures: $MO_x$ Receptor's Role in Gas Detection. *Sensors* **2025**, *25*, 376. https://doi.org/10.3390/s25020376



## 1. Introduction

The most common approaches to improve the sensitivity, selectivity, and stability of semiconductor gas sensors are: (i) technological, involving the use of preconcentrators and active or passive filters; (ii) operational, using operating temperature modulation modes or additional measured parameters; and (iii) chemometric, including various data processing algorithms. The fundamental chemical approach is based on the complication of the composition of semiconductor metal oxides forming a sensitive layer, which can be implemented through the introduction of additives providing surface functionalization, bulk doping, and the creation of multiphase nanocomposites combining two or more semiconductor oxides ($M^IO/M^{II}O$) sensing material. It is known that semiconducting oxides of the *n* and *p*-type of conductivity are characterized by various sensor properties due to differences in the M-$O_{lat}$ [1,2] metal–oxygen bond strength and MO-$O_{ads}$ [3] chemisorbed oxygen bond energy. Depending on the $M^I$ and $M^{II}$ nature, $M^I/M^{II}$ mole ratio, and structural features as well as $M^IO$ and $M^{II}O$ electrical behavior, the formation of different types of nanocomposites is possible: (i) a solid solution $(M^IO)_x(M^{II}O)_{1-x}$ due to the mutual diffusion of components, (ii) a structure with a sharp *n-n* or *n-p* barriers in the heterojunction region, and (iii) a structure including complex phases $M^IM^{II}O_y$ appearing at the interface as a result of the chemical interaction of the $M^IO$ and $M^{II}O$ metal oxides [4–9].

The review article [10] considers the concepts that are currently used to explain the mechanisms by which the effect of additives on the characteristics of semiconductor

materials formed by oxide nanoparticles arranged in a porous layer is realized. The authors discuss various chemical and/or electrical factors that ensure a change in the sensitivity and selectivity of semiconductor materials, mainly in cases where noble metal nanoparticles act as additives. Of course, the concepts presented can generally be applied to combinations of semiconductor metal oxides and a wide range of additives. However, because they possess different adsorption capabilities and reactivities when interacting with gases, the components of the composite can significantly affect the complex acid–base and oxidation–reduction processes, which determine the sensitivity and selectivity of a sensing material [2]. There are some reviews concerning the sensor properties of composites or heterostructures based on metal oxides [11–15]. However, the difference in the metal oxide nature and morphology, methods of synthesis, and detected gases does not allow us to represent the regularities of the structure and sensor properties of $M^{I}O/M^{II}O$ materials.

This work presents the results of an investigation into the structural, electrical, and sensor properties of composites obtained under the same conditions using the co-electrospinning method based on ZnO nanofibers modified with 15 mol% $MO_x$ (M = $Fe^{III}$, $Co^{II,III}$, $Ni^{II}$, $Ga^{III}$, $In^{III}$, $Sn^{IV}$; [M]/([Zn] + [M]) = 15 mol%) forming complex phases $M^{I}M^{II}O_y$ of *n*- or *p*-type. The difference in the $MO_x$-$O_{ads}$ chemisorbed oxygen bond energy and band structure of the $MO_x$ component allows for the variation of the electrophysical and sensor properties of nanocomposites. The sensor signal (*S*) was measured depending on the temperature of 60–500 °C toward air pollutants, including reducing the gases CO, methanol, and acetone and oxidizing the gas $NO_2$. The temperature corresponding to the maximum sensor signal ($T_{max}$) was compared for different modifiers ($MO_x$) as a characteristic of the reactivity of nanofiber heterostructures when interacting with gases.

## 2. Materials and Methods

### *2.1. Materials Synthesis*

Nanofibers of ZnO and ZnO/$MO_x$ (M = $Fe^{III}$, $Co^{II,III}$, $Ni^{II}$, $Ga^{III}$, $In^{III}$, $Sn^{IV}$) were prepared by co-electrospinning the corresponding salt organic solutions in polyvinylpyrrolidone (PVP, M = 1,300,000) followed by heat treatment of the polymer to remove and metal oxide crystallization. For fiber fabrication, the analytical pure-grade precursors were used (Table 1). The composition of polymer solutions was chosen to reach the same concentration of 15 mol% ([M]/([Zn] + [M])) in all the heterostructures after annealing. The ratio of [M]/([M] + [Zn]) = 15 mol% was chosen based on our previous studies of ZnO/Co composites with different cobalt contents, where this particular composition showed the best properties for use as a sensor material for detecting both oxidizing and reducing gases in a resistance level, sensor response in dry and humid air, and dynamic properties [16]. The electrospinning of polymer solution was carried out at the conditions of 1 mL/h solution feed rate, with a 125 mm distance and 12 kV voltage between the needle and metal collector. The fibrous material was heated at 550 °C (5 h) in air. The annealing conditions for polymer decomposition were determined using thermogravimetric analysis with mass spectral analysis of gaseous products (TG-MS) using a NETZSCH STA 09 PC/PG instrument (Netzsch-Gerätebau GmbH, Selb, Germany).

**Table 1.** Composition and microstructure parameters of ZnO and ZnO/$MO_x$ nanofibers.

| Sample | $MO_x$ Precursor | M/(Zn + M) [1], mol% (XRF) | Phase Composition (XRD) | $d_{XRD}$ [2], nm | Morphology |
|---|---|---|---|---|---|
| ZnO | - | - | ZnO (wurtzite) | 14 ± 1 | fibers |
| ZnO/Co | $Co(CH_3COO)_2 \cdot 4H_2O$ | 15.3 ± 0.8 | ZnO (wurtzite);<br>$Zn_xCo_{3-x}O_4$ (cubic) | 15 ± 1<br>12 ± 1 | tubes |
| ZnO/Ni | $Ni(NO_3)_2 \cdot 6H_2O$ | 16 ± 1 | ZnO (wurtzite);<br>$Zn_xNi_{1-x}O$ (cubic) | 16 ± 1<br>10 ± 1 | tubes |
| ZnO/Fe | $Fe(acac)_3$ | 15.0 ± 0.9 | ZnO (wurtzite);<br>$ZnFe_2O_4$ (cubic) | 11 ± 1<br>9 ± 1 | fibers |
| ZnO/Sn | $SnCl_4 \cdot 5H_2O$ | 14.3 ± 0.8 | ZnO (wurtzite);<br>$SnO_2$ (tetragonal);<br>$Zn_2SnO_4$ (cubic) | 26 ± 2<br>13 ± 1<br>- | fibers |
| ZnO/In | $In(NO_3)_3 \cdot 4.5H_2O$ | 14.8 ± 0.8 | ZnO (wurtzite);<br>$In_2O_3$ (cubic) | 10 ± 1<br>10 ± 1 | tubes |
| ZnO/Ga | $Ga(NO_3)_3 \cdot 9H_2O$ | 14.6 ± 0.9 | ZnO (wurtzite);<br>$ZnGa_2O_4$ (cubic) | 10 ± 1<br>9 ± 1 | fibers |

[1] Content of the second component determined with X-ray fluorescence analysis. [2] Size of the coherent scattering region determined from the broadening of diffraction peaks using Scherrer equation.

### *2.2. Materials Characterization*

The phase composition of nanofiber was determined with X-ray powder diffraction (XRD) using a DRON-4 diffractometer and Cu Kα radiation (λ = 1.5418 Å). The crystallite size ($d_{XRD}$) was calculated with the Scherrer equation using the full width of half the maximum of the most intense peaks. The chemical composition of samples was studied by X-ray fluorescence (XRF) method using an M1 Mistral X-ray spectrometer (Bruker Nano GmbH, Berlin, Germany). The analyzed area was 1.5 mm, the measurements were carried out at a voltage of 50 kV, and the signal accumulation time was 5 min. Examples of the spectra are shown in Figure S1 (Supporting Information). The results were averaged over three points. The electronic state of modifiers was analyzed using X-ray photoelectron spectroscopy (XPS) using an Axis Ultra DLD (Kratos) spectrometer with an Al $K_\alpha$ source. The binding energy was calibrated with a C 1 s peak at 285.0 eV. The XP spectra of the Ga3d, Sn3d, In3d, Co2p, Fe2p, and Ni2p regions and their interpretation are presented in Figure S2 and Table S1, respectively (Supporting Information). The morphology of the nanofibers was studied with scanning electron microscopy (SEM) using a Carl Zeiss NVision 40 electron microscope (Carl Zeiss NTS GmBH, Oberkochen, Germany) at 5 kV. Sample characteristics are summarized in Table 1.

### *2.3. Gas Sensing Measurements*

Thick film (~150 μm, Figure 1) gas sensors of the resistive type based on ZnO/$MO_x$ nanofibers were fabricated on alumina substrates embedded in a TO-8 package and provided with Pt electrodes (size 0.3 × 0.2 mm, gap 0.2 mm) and a Pt heater. Powders were dispersed in terpineol and drop-deposited with a micropipette. The sensors were placed in a flow chamber equipped with a PC temperature controller and electrometer. Thick films were heated at 450 °C for 5 h to remove the organic binder.

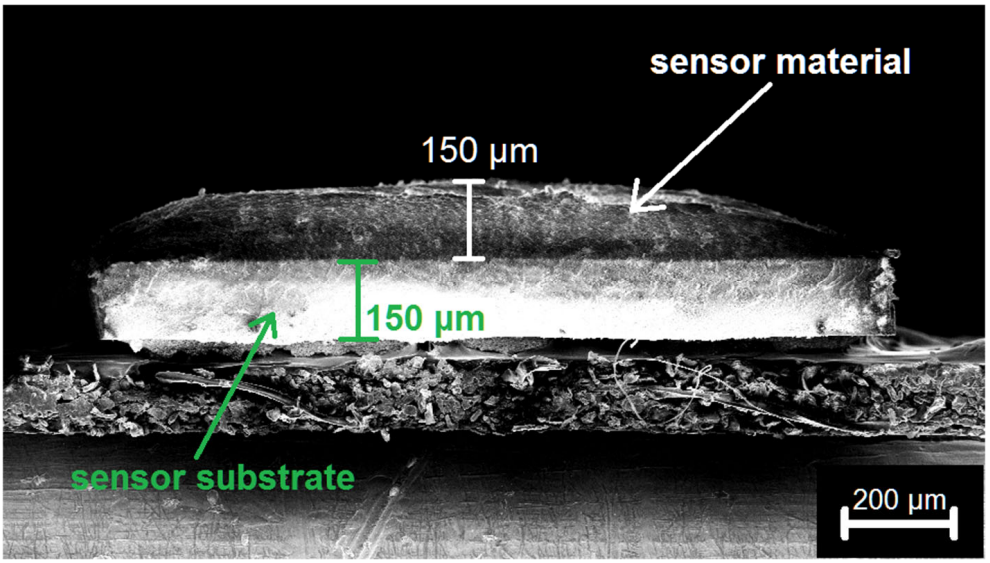


**Figure 1.** SEM image of thick film formed on alumina substrates.

The sensor properties were investigated using laboratory-made equipment of an original design, which enables the measurement of the resistance in the range of $10^1$–$10^{11}$ Ohms (at a voltage of no more than 1 V) in the controlled temperature range of 20–600 °C. The unit allows the flow rate of the gas mixture to be maintained through the Teflon chamber in the range of 0–300 mL/min and to humidify the gas mixture in the range of RH = 0–90%. DC resistance was measured with the applied voltage 1 V at a temperature range of 60–500 °C. The carrier gas was pure air from a pure air generator model "2,0–3,5" (Himelectronica, Moscow, Russia). The contamination level was within the limits of 10 ppm $H_2O$, 2 ppm $CO_2$, and 0.1 ppm hydrocarbons. Certified gas mixtures were used as the sources of target gases: 2560 ppm CO, 745 ppm $C_3H_6O$, 1520 ppm $CH_3OH$, and 96 ppm $NO_2$ (all in $N_2$) (Monitoring, Saint-Petersburg, Russia). Gas flows were controlled with mass-flow controllers EL-FLOW (Bronkhorst, Gelderland, the Netherlands). During the exposure of sensors to the background gas, pure air was purged with a flow rate of 100.0 mL/min. The dilution of a target gas to the desired concentration was performed by mixing the flow of a target gas (flow rate 0.1–10 mL/min) with the flow of pure air (flow rate reduced to 99.9–90.0 mL/min). The sensor signal $S$ was defined as the ratio of resistance change:

$$S = \frac{R_g}{R_a} - 1 \text{ for the oxidizing gas} NO_2 \quad (1)$$

$$S = \frac{R_a}{R_g} - 1 \text{ for the reducing gases CO}, C_3H_6O, CH_3OH \quad (2)$$

where $R_a$ is the sensor's resistance in air, and $R_g$ is the sensor's resistance in the target gas.

## 3. Results and Discussion

### *3.1. Composition and Microstructure Characterization*

It is known [17–19] that the sensitivity of thick films of sensor elements can be controlled by both surface reactions and gas diffusion through the sensitive layer. To highlight the role of various modifiers in the formation of the sensor response of zinc oxide-based nanocomposites and to avoid the effect of gas diffusion, we compared the properties of thick film sensors obtained under strictly identical conditions in order to minimize the influence of other characteristics such as film thickness, crystallite size, and specific surface area.

The total concentrations of modifiers in $ZnO/MO_x$ samples determined with X-ray fluorescence spectroscopy coincide with those set during synthesis within the limits of the analysis error (Table 1). X-ray diffraction data presented in Figure 2 demonstrate that $ZnO/MO_x$ samples, except for the ZnO/Sn, contain two crystalline phases (Table 1): zinc oxide with wurtzite structure (ICDD [36-1451]) and the phase of a simple or complex oxide related to MO. The phase composition of the ZnO/Sn sample is more complex and contains three phases: zinc oxide with wurtzite structure (ICDD [36-1451]), tin oxide with rutile structure (ICDD [41-1445]), and zinc orthostannate $Zn_2SnO_4$ (ICDD [24-1470]). The assumption about the presence of the $ZnGa_2O_4$ phase in the ZnO/Ga sample is based on an asymmetric broadening of the (101) wurtzite diffraction maximum ($2\theta = 36.25°$) detected through detailed profile analysis of ZnO and ZnO/Ga diffraction patterns (Figures S3 and S4, Supporting Information).

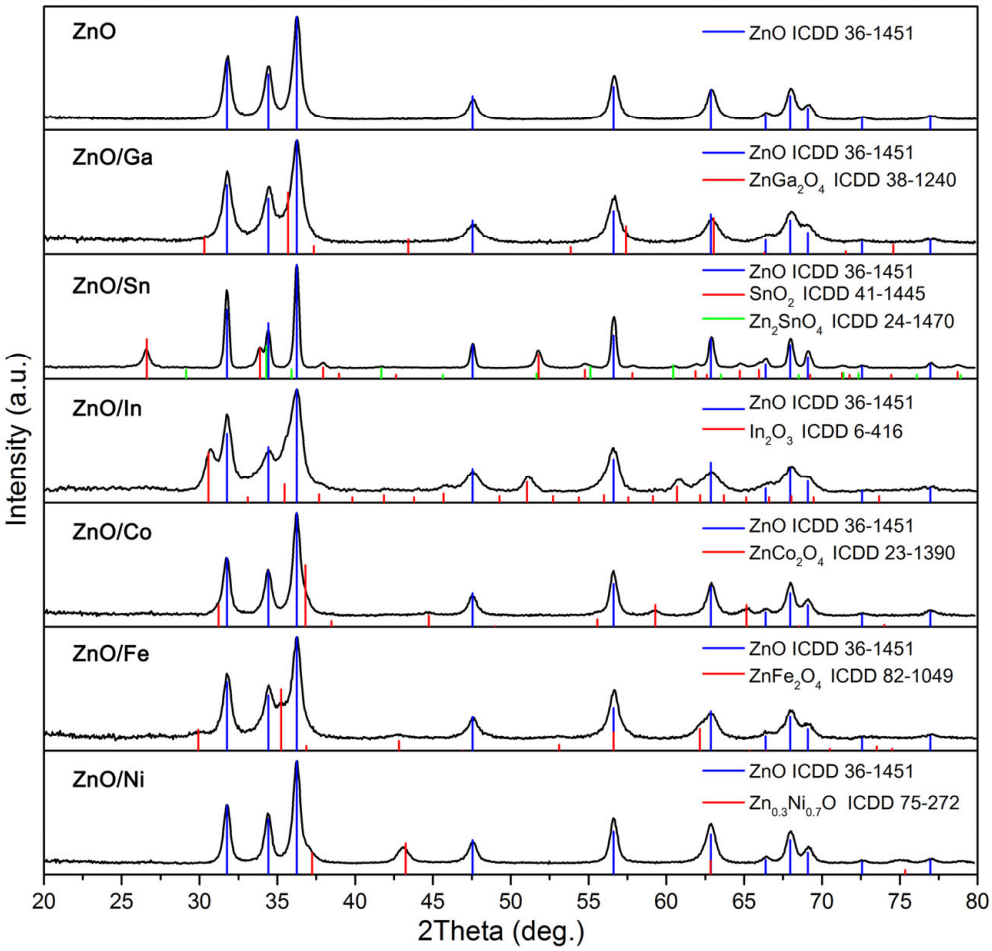


**Figure 2.** Powder X-ray diffraction patterns of ZnO and $ZnO/MO_x$ samples.

According to the scanning electron microscopy (SEM) data, all samples are three-dimensional, highly porous spongy structures consisting of polycrystalline nanofibers longer than 10 μm (Figure 3). Fibers of ZnO/In, ZnO/Co, and ZnO/Ni heterostructures form tubes with a diameter of 80–100 nm that may be caused by the difference in the rates of crystallization of ZnO and $MO_x$ oxides and mutual diffusion of components. From the low-temperature nitrogen adsorption data, the specific surface area of all samples is about 13–15 $m^2/g$.

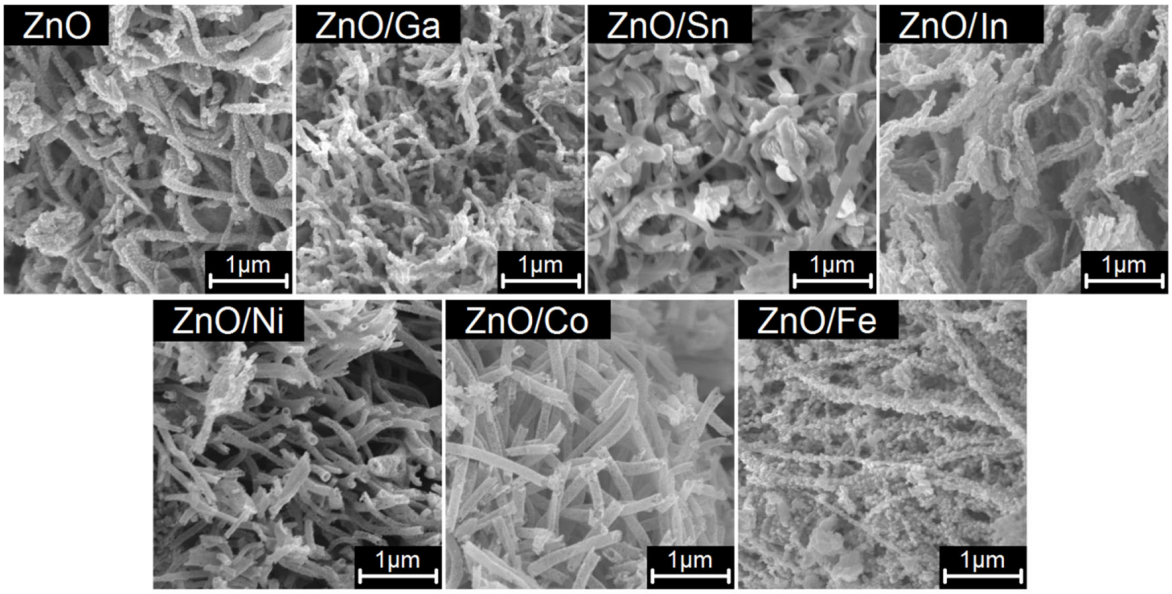


**Figure 3.** SEM images of ZnO and ZnO/$MO_x$ samples.

### *3.2. Electrical Conductivity Measurements*

Figure 4 shows the temperature dependence of the ZnO/$MO_x$ conductivity. All measurements were carried out with a stepwise decrease in temperature. The resistance of the ZnO/Co, ZnO/Fe, and ZnO/Ni samples in the entire temperature range is 2–3 orders of magnitude higher relative to the ZnO, ZnO/Ga, ZnO/Sn, and ZnO/In samples that may be associated with the formation of a significant barrier at the grain interface in samples ZnO/Co, ZnO/Fe, and ZnO/Ni. Formed at the interface complex oxides containing modifier cations: $ZnCo_2O_4$ (work function $\varphi$ = 5.6 eV [20], $ZnFe_2O_4$ ($\varphi$ = 5.46 eV [21]), and $Zn_xNi_{1-x}O$ ($\varphi$ = 6.3 eV for NiO [22]) have *p*-type conductivity, while ZnO ($\varphi$ = 5.2 eV [23]), $ZnGa_2O_4$ ($\varphi$ = 3.54 eV [24]), $SnO_2$ ($\varphi$ = 4.7 eV [25]), and $In_2O_3$ ($\varphi$ = 4.3 eV [26]) are characterized by *n*-type conductivity. The high conductivity of ZnO/Ga, ZnO/Sn, and ZnO/In heterostructures can be due to the electron accumulation layer formed in ZnO grains and the effect of doping zinc oxide, for which In, Ga, and Sn are the effective donor impurities. At low temperatures of 100–300 °C, the conductivity behavior is complex and does not linearize in the lnG-(1/T) coordinates due to oxygen adsorption/desorption on the surface of semiconductor oxides. These processes are accompanied by the capture and delocalization of electrons in the near-surface layer and affect the conductivity of the materials. Additionally, a comparison of the temperature dependences of ZnO/$MO_x$ electrical conductivity in dry air and in dry nitrogen is shown in Figure S5 (Supporting Information). The electrical conductivity of materials in dry nitrogen always exceeds the electrical conductivity in dry air. It can be noted that this difference tends to increase with decreasing temperature, which indicates an increased contribution of oxygen adsorption on the semiconductor surface in the low-temperature region.

In the range of 350–500 °C, the temperature dependences of the conductivity are linearized in lnG-(1/T) coordinates, which indicates that conductivity has an activation mechanism. The activation energy $E_a$ of conductivity for ZnO/Co, ZnO/Fe, and ZnO/Ni composites with *p-n* heterojunctions is higher than that for ZnO/Ga, ZnO/Sn, and ZnO/In samples with *n-n* heterojunction and pure ZnO (Table 2). This effect can be explained using a model of an inhomogeneous semiconductor with large-scale potential fluctuations, which consists of a smooth band's bending with the formation of a random potential barrier caused by the potential of charged impurities [27]. According to this model, the movement of an electron is impossible in a modulated zone if its energy is below a certain

level necessary to overcome barriers (mobility threshold level), which is determined by the nature of the potential relief. Thus, the energy determined from the temperature dependences of the conductivity is the energy necessary for the carrier's activation from the Fermi level to the mobility threshold level. The increase in the activation energy of conductivity for composites with *p-n* heterocontacts is probably due to the formation of a larger potential barrier at the *p-n* ZnO/$MO_x$ interface compared to *n-n* heterostructures. This leads to a larger-scale modulation of the band's relief that increases the mobility threshold level and, accordingly, the activation energy of the conductivity.

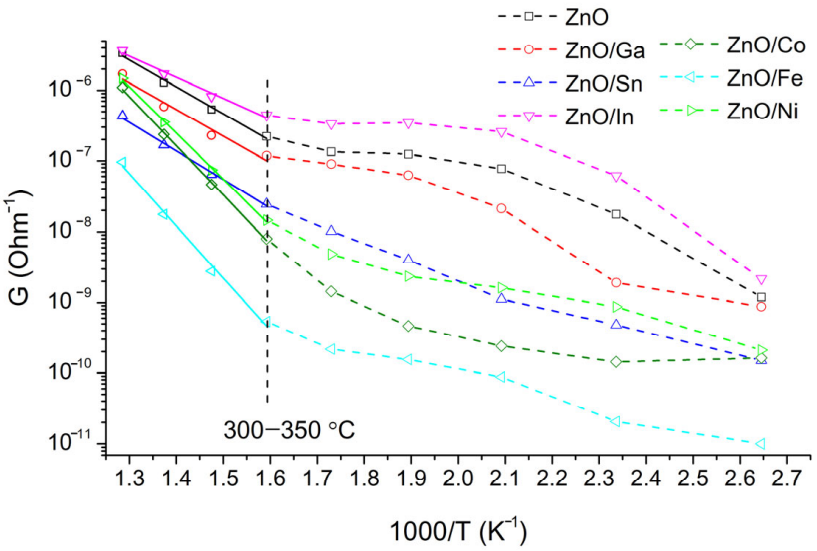


**Figure 4.** Temperature dependences of ZnO/$MO_x$ conductivity in dry air.

**Table 2.** Activation energy of conductivity ($E_a$) and difference in the electron work functions $\varphi$(MO) − $\varphi$(ZnO) for ZnO and ZnO/$MO_x$ nanofibers.

| Sample | $MO_x$ Phase [1] | $E_a$, eV (T = 350–500 °C) | $\varphi$(MO) − $\varphi$(ZnO), eV |
|---|---|---|---|
| ZnO | - | 0.46 | - |
| ZnO/Co | $ZnCo_2O_4$ | 0.84 | 0.4 |
| ZnO/Ni | NiO | 0.79 | 1.1 |
| ZnO/Fe | $ZnFe_2O_4$ | 0.89 | 0.26 |
| ZnO/Sn | $SnO_2$ | 0.49 | −0.5 |
| ZnO/In | $In_2O_3$ | 0.36 | −0.9 |
| ZnO/Ga | $ZnGa_2O_4$ | 0.45 | −1.66 |

[1] The work function value $\varphi$ for this phase is used.

### *3.3. Gas Sensor Measurements*

#### 3.3.1. Detection of Reducing Gases

The sensor properties of ZnO/$MO_x$ nanofibers were studied when detecting the reducing gases CO (20 ppm), acetone (20 ppm), and methanol (20 ppm) in the temperature range of 60–500 °C. The dynamic response of the material resistance to the introduction of 20 ppm of CO into background dry air depending on temperature is shown in Figure 5a. As illustrated in Figure 5b–d, ZnO/$MO_x$ nanofibers are characterized by different temperature dependences of the sensor signal. When detecting reducing gases, *p-n* heterostructures ZnO/Co and ZnO/Ni demonstrate maximum sensor response at lower temperatures compared to ZnO and *n-n* heterostructures ZnO/In, ZnO/Ga and ZnO/Sn.

Differences in the sensor response of *n*-type and *p*-type semiconductor oxides, as well as nanocomposites with *p-n* heterojunctions, due to different mechanisms of electrical conductivity, are discussed in [10,28,29], respectively. The main parameters responsible for

the sensor response value are the initial band bending, which is determined by the ratio of the concentration of charge carriers near the surface and in the bulk of crystallites, as well as morphological parameter determined by the average grain size and the contact size [29]. Taking into account that the morphological parameter does not differ for the considered ZnO/MOx nanofibers, it can be assumed that the sensor response is determined by the initial band bending and its change depending on the temperature and surface reactivity of *n*-type and *p*-type components when interacting with oxygen.

The difference in the temperature of the maximum sensor response $T_{max}$ when detecting reducing gases can be discussed based on the binding energies of chemisorbed oxygen E(MO-$O_{ads}$). The binding energy between the surface of some binary metal oxides and chemisorbed oxygen is shown in Figure 6, according to Boreskov's works [30]. Figure 7 demonstrates for ZnO/$MO_x$ nanofibers the dependences of the temperature of the maximum sensor signal $T_{max}$ toward CO, acetone, and methanol on the binding energy of chemisorbed oxygen for binary metal oxides containing modifier cations.

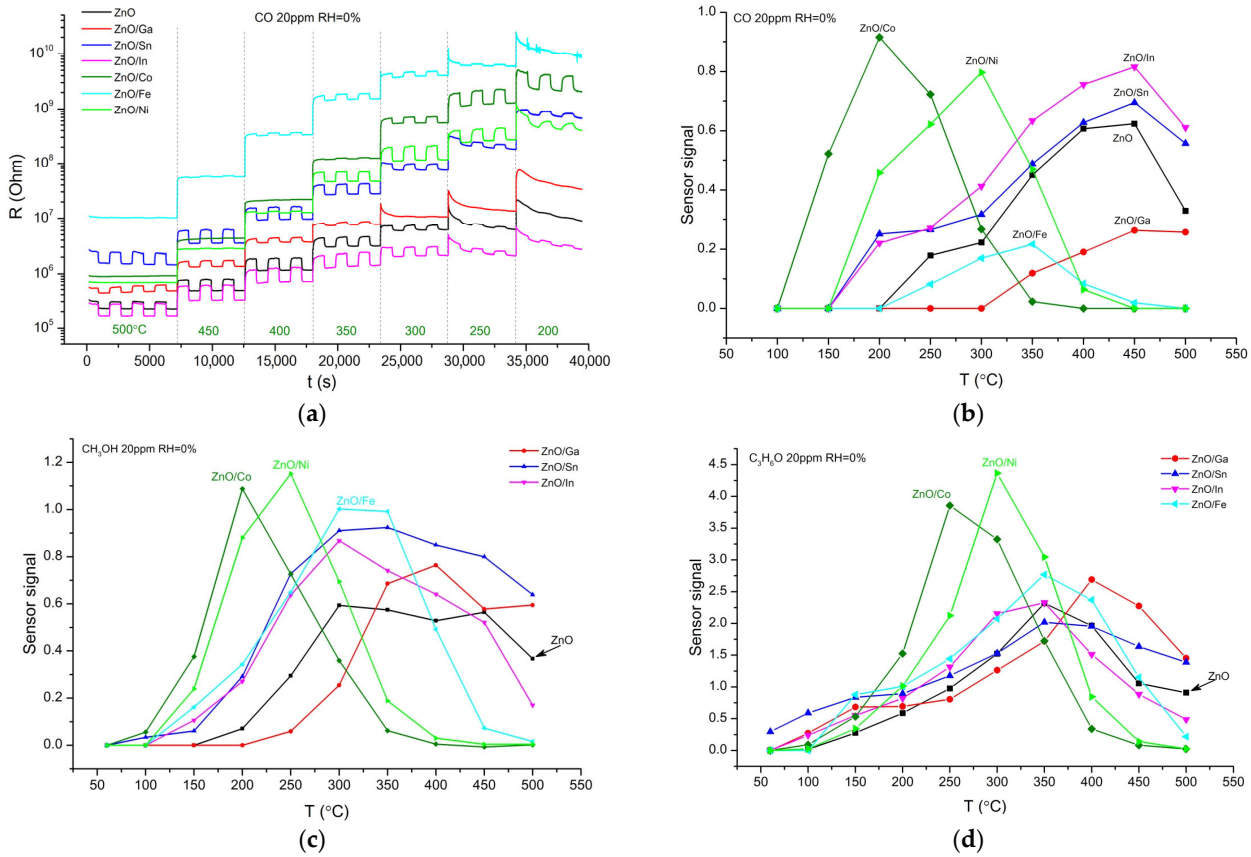


**Figure 5.** Dynamic change of the resistance of ZnO/$MO_x$ nanofibers when detecting 20 ppm CO in dry air at different working temperatures (**a**). Temperature dependences of the sensor response of ZnO/$MO_x$ nanofibers when detecting 20 ppm CO (**b**), 20 ppm methanol (**c**), and 20 ppm acetone (**d**) in dry air.

In the case of methanol and acetone, in general, one can note a tendency to increase $T_{max}$ with an increase in E(MO-$O_{ads}$). In particular, $Co_3O_4$ and NiO are characterized by the weakest binding energy of chemisorbed oxygen with the oxide's surface that, for ZnO/Co and ZnO/Ni samples, can explain high sensor signal and low $T_{max}$ when interacting with reducing gases by the following reaction:

$$\beta \cdot R_{(gas)} + O^{\alpha-}_{\beta(ads)} \rightarrow \beta \cdot RO_{(gas)} + \alpha \cdot e^{-}, \quad (3)$$

where $O^{\alpha-}_{\beta(ads)}$ is chemisorbed oxygen species, $RO_{(gas)}$ is the product of the oxidation of reducing gas $R_{(gas)}$, and $e^-$ is a free electron.

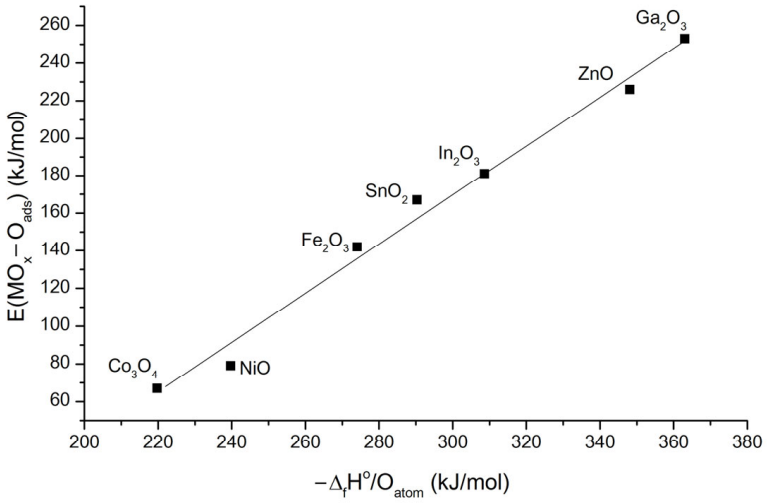


**Figure 6.** Correlation of the binding energy of adsorbed oxygen with the surface of the oxide $E_{MOx}$-$O_{ads}$ and the energy of oxide formation attributed to the number of oxygen atoms in the oxide $-\Delta_f H^\circ / O_{atom}$ [1,31].

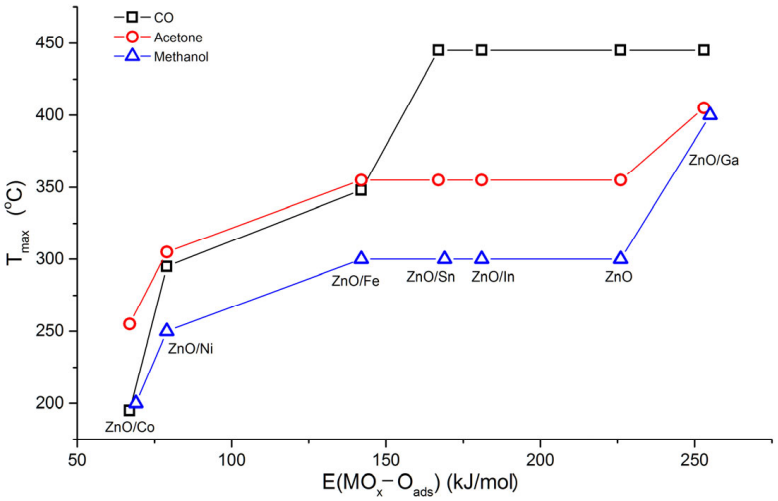


**Figure 7.** Temperature of the maximum sensor signal $T_{max}$ of ZnO/$MO_x$ nanofibers when detecting CO, acetone, and methanol (all 20 ppm in dry air) on the binding energy of chemisorbed oxygen for binary metal oxides containing modifier cations.

The values of the maximum sensor response of ZnO and *n-n* heterostructures ZnO/Ga, ZnO/In, and ZnO/Sn toward methanol (Figure 5c) demonstrate an upward trend with an increase in the Lewis acidity $A_L$ of oxides in the raw ZnO ($A_L$ = 1.6) < $Ga_2O_3$ ($A_L$ = 2.5) < $In_2O_3$ ($A_L$ = 2.6) < $SnO_2$ ($A_L$ = 3.5) [32]. It can be assumed that Lewis acid sites at the surface of semiconductor metal oxides serve as adsorption sites for $CH_3OH$ molecules and, thus, favor the oxidation of target molecules at appropriate temperatures [1].

In the case of acetone detection (Figure 5d), no correlation was observed between sensor signals and Lewis acidity of ZnO and *n-n* heterostructures. It suggests that the determining factor for the sensor response should be the reactivity of the materials surface in oxidation Reaction (3) [2]. The difference in the sensor response values may be due, among other things, to the inequality in the predominant form of chemisorbed oxygen $O^{\alpha-}_{\beta(ads)}$, which at a fixed temperature is determined by the composition and microstructure parameters of the semiconductor oxide [33].

When detecting CO, ZnO/$MO_x$ nanofibers can be divided into two groups. For composites with *p-n* heterojunctions, $T_{max}$ increases with E(MO-$O_{ads}$), while for ZnO and composites with *n-n* heterojunctions, the temperature of the maximum sensor signal is much higher (about 400–450 °C) and practically does not depend on the binding energy of chemisorbed oxygen. This effect becomes clear if one takes into account that the sensor response of unmodified ZnO when detecting CO in dry air is due to CO oxidation by chemisorbed oxygen $O^{\alpha-}_{\beta(ads)}$ (Reaction (3)) and lattice oxygen $O_{lat}$ (Reaction (4)) (Mars–van Krevelen mechanism) [34]:

$$CO_{(gas)} + O_{lat} \rightarrow CO_{2(gas)} + V_O^{2+} + 2e^-, \quad (4)$$

where $V_O^{2+}$ is the doubly ionized oxygen vacancy in the ZnO lattice.

Since ZnO is the dominant phase in ZnO/$MO_x$ nanofibers, and the modifier does not possess a sufficiently low binding energy with chemisorbed oxygen, it can be assumed that the main contribution to the sensor response is made by the CO oxidation by ZnO lattice oxygen that determines such a high $T_{max}$ value.

#### 3.3.2. Detection of Oxidizing Gases

The presence of $NO_2$ in dry air leads to an increase in the resistance of all materials because $NO_2$ molecules are electron acceptors and act as electron traps upon adsorption on the metal oxide surface. The mechanism of $NO_2$ detection is based on ionosorption of analyte molecules to form surface nitrites $NO^-_{2(ads)}$:

$$NO_{2(gas)} + e^- \rightarrow NO^-_{2(ads)} \quad (5)$$

which undergoes disproportionation and/or conversion, resulting in $NO^-_{3(ads)}$, $NO^+_{(ads)}$, etc. [2]. The authors of [35] showed using Raman spectroscopy that the electrical conductivity of *n*-type $SnO_2$ in the presence of $NO_2$ correlates with the concentration of surface bidentate nitrite groups. Ab initio calculations [36] indicate that the most energetically advantageous is the molecular adsorption of nitrogen dioxide with the coordination of one or both oxygen atoms of the $NO_2$ molecule on the vacancies of bridging oxygen atoms of the partially reduced tin dioxide surface. IR spectroscopy and programmable thermal desorption in the temperature range of 25–400 °C [37] have shown the possibility of $NO_2$ dissociation upon interaction with the surface of tin dioxide. The presence of NO molecules in the thermal desorption products may serve as indirect evidence of the following reaction:

$$NO_{2(ads)} \rightarrow NO_{(gas)} + O^-_{(ads)} \quad (6)$$

The typical sites for $NO_2$ adsorption on the ZnO surface are oxygen vacancies, on which, according to XPS and IR studies, near room temperature, a $NO_2$ molecule can orient itself in different ways, with the formation of $NO_2^-$ and $NO_3^-$ ions [38–44]. In situ mass spectrometry study of the photostimulated interaction of $O_2$ and $NO_2$ molecules with the ZnO surface under UV radiation in the temperature range of 30–100 °C demonstrated that the sensor response to $NO_2$ requires both unoccupied adsorption sites and free electrons that can be expressed by the following equations [45]:

$$NO_{2(gas)} + V_O + e^- \rightarrow NO_2^- \ldots V_O \quad (7)$$

$$NO_{2(gas)} + O_{lat} + V_O + e^- \rightarrow NO_3^- \ldots V_O \quad (8)$$

Figure 8 shows the temperature dependences of the sensor signal *S* of ZnO and ZnO/$MO_x$ nanofibers toward 1 ppm $NO_2$ in dry air in the temperature range of 80–500 °C.

The ZnO/Ga and ZnO/In composites demonstrate the highest sensor signal at a temperature of 100 °C that may be associated with the doping effect of $Ga^{3+}$ and $In^{3+}$ cations in ZnO leading to an increase in the concentration of donor defects—oxygen vacancies and free electrons favoring Reaction (5) [2,46].

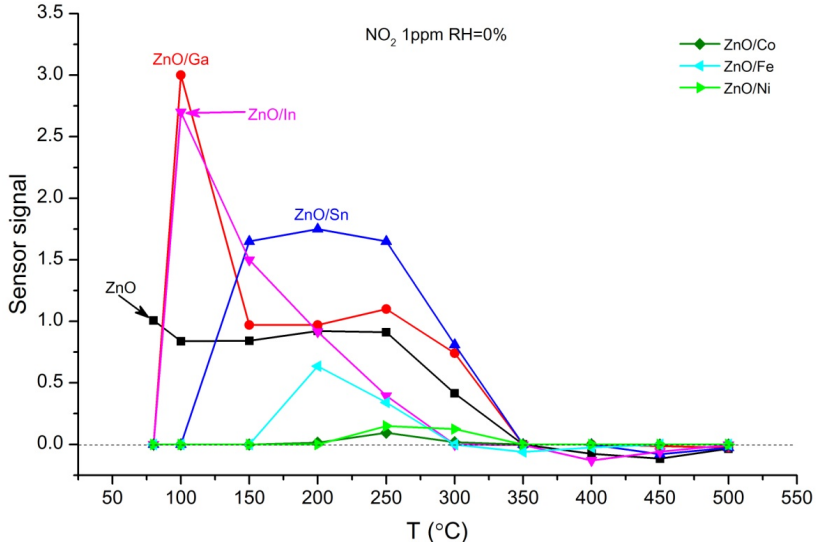


**Figure 8.** Temperature dependences of the sensor response of $ZnO/MO_x$ nanofibers when detecting 1 ppm $NO_2$ in dry air.

Since the formation of the sensor response of semiconductor metal oxides toward oxidizing gases is due to the localization of free electrons and, accordingly, depends on the concentration of electrons in the near-surface layer, the maximum sensor signal *S* and the temperature of the maximum sensor signal $T_{max}$ may depend on the potential barrier at the interface between ZnO and a complex oxide containing a modifier. The band bending at the $ZnO/MO_x$ interface can be characterized by the difference in the electron work function as $\varphi(MO) - \varphi(ZnO)$. The dependence of S and $T_{max}$ values on band bending in $ZnO/MO_x$ nanofibers is shown in Figure 9.

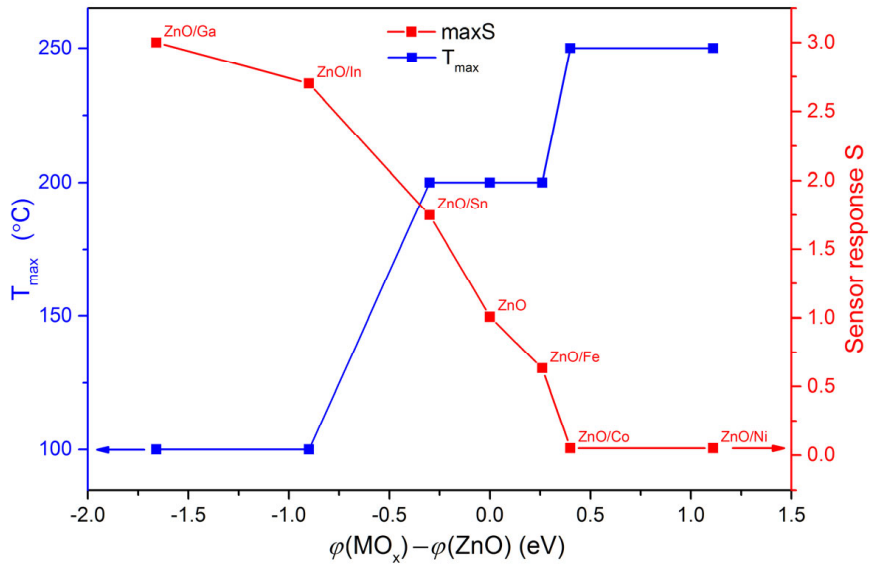


**Figure 9.** Maximum sensor response S and temperature of the maximum sensor signal $T_{max}$ of $ZnO/MO_x$ nanofibers when detecting 1 ppm $NO_2$ in dry air vs. the band bending in $ZnO/MO_x$ nanofibers.

It follows from Figure 9 that the maximum sensor response S, as well as the temperature of the maximum sensor signal $T_{max}$ when detecting 1 ppm $NO_2$ in dry air, monotonously, but oppositely directed, changes with the band bending in $ZnO/MO_x$ nanofibers. Thus, as the band bending decreases, the sensor signal increases, and the temperature of the maximum sensor signal decreases. The formation of a heterocontact between ZnO and a semiconductor with a larger work function leads to the electron depletion of the near-surface of ZnO grains, which causes a decrease in the sensor response of the composite. On the contrary, when forming a heterocontact between ZnO and a semiconductor with a smaller work function, the concentration of electrons in the near-surface layer of ZnO grains increases, providing an increase in sensor response. The temperature corresponding to the maximum sensor signal of $ZnO/MO_x$ nanocomposites toward $NO_2$ correlates with the value of the activation energy of conductivity, discussed in Section 3.2 (Table 2). In the case of composites with a *p-n* heterocontact, a higher temperature is necessary for the electrons to overcome the activation barrier of conductivity and form a significant electrical response.

## 4. Conclusions

The introduction of M = $Fe^{III}$, $Co^{II,III}$, $Ni^{II}$, $Sn^{IV}$, $In^{III}$, and $Ga^{III}$ modifiers into ZnO nanofibers in the co-electrospinning synthesis leads to the formation of multiphase $ZnO/MO_x$ nanocomposites containing ZnO with a wurtzite structure and a complex oxide including modifier cations. The study of the sensor properties of ZnO and $ZnO/MO_x$ nanofibers when detecting reducing gases CO, methanol, and acetone showed that low binding energy of chemisorbed oxygen with the surface of the modifier's oxides determines the high sensitivity of materials toward reducing gases in the low temperature range of 200–300 °C. When detecting oxidizing gases, for example, $NO_2$, the most important condition for achieving high sensitivity is a high concentration of donor active sites and free electrons in the near-surface layer, which is associated with the band bending at the $ZnO/MO_x$ interface characterized by the difference in the electron work function of ZnO and $MO_x$. Nanocomposites ZnO/Ga, ZnO/In, and Zn/Sn, in which the electron work function of the $MO_x$ is smaller than the corresponding value for zinc oxide, demonstrate high sensitivity toward $NO_2$ at temperatures of 100–200 °C.

**Supplementary Materials:** The following supporting information can be downloaded at: https://www.mdpi.com/article/10.3390/s25020376/s1, Figure S1. XRF spectra of unmodified ZnO and ZnO/MOx nanofibers; Figure S2. XP spectra of modifiers in $ZnO/MO_x$; Figure S3. XRD patterns of ZnO and ZnO/Ga showing the presence of the $ZnGa_2O_4$ phase in ZnO/Ga; Figure S4. Profile analysis of ZnO/Ga diffraction pattern sample without (a) and with additional reflection from $ZnGa_2O_4$ phase (b); Figure S5. Comparison of the temperature dependences of ZnO/MOx electrical conductivity in dry air and in dry nitrogen; Table S1. Interpretation of XP spectra of ZnO/MOx nanofibers.

**Author Contributions:** Conceptualization, M.R.; methodology, V.P. and M.R.; formal analysis, V.P. and M.R.; investigation, V.P.; resources, O.S.; data curation, V.P.; writing—original draft preparation, V.P. and M.R.; writing—review and editing, V.P., O.S. and M.R.; project administration, O.S.; funding acquisition, O.S. All authors have read and agreed to the published version of the manuscript.

**Funding:** This research was funded by a grant from the Ministry of Science and Higher Education of the Russian Federation, grant number 075-15-2024-646.

**Institutional Review Board Statement:** Not applicable.

**Informed Consent Statement:** Not applicable.

**Data Availability Statement:** The original contributions presented in the study are included in the article. Further inquiries can be directed to the corresponding author.

**Acknowledgments:** SEM studies were performed at the Centre of Shared Equipment of IGIC RAS. Verification of $NO_2$ concentration (Teledyne API N500 CAPS NOX Analyzer) was performed using the equipment purchased through the Lomonosov Moscow State University Program of Development.

**Conflicts of Interest:** The authors declare no conflicts of interest.

## References

1. Marikutsa, A.; Novikova, A.; Rumyantseva, M.; Khmelevsky, N.; Gaskov, A. Comparison of Au-functionalized semiconductor metal oxides in sensitivity to VOC. *Sens. Actuators B* **2021**, *326*, 128980. [CrossRef]
2. Marikutsa, A.; Rumyantseva, M.; Konstantinova, E.; Gaskov, A. The key role of active sites in the development of selective metal oxide sensor materials. *Sensors* **2021**, *21*, 2554. [CrossRef] [PubMed]
3. Christensen, J.M.; Grunwaldt, J.-D.; Jensen, A.D. Importance of the oxygen bond strength for catalytic activity in soot oxidation. *Appl. Catal. B* **2016**, *188*, 235–244. [CrossRef]
4. Korotcenkov, G.; Cho, B.K. Metal oxide composites in conductometric gas sensors: Achievements and challenges. *Sens. Actuators B* **2017**, *244*, 182–210. [CrossRef]
5. Zhang, L.; Li, F.; Yang, Y.; Li, D.; Yu, H.; Dong, X.; Wang, T. Polyoxometalates/metal–organic frameworks-derived $ZnO/ZnWO_4$ nanoparticles for highly sensitive and selective ppb-level $NO_2$ detection. *Chem. Eng. J.* **2024**, *499*, 156604. [CrossRef]
6. Zhang, L.; Tian, J.; Wang, Y.; Wang, T.; Wei, M.; Li, F.; Dan Li, D.; Yang, Y.; Yu, H.; Dong, D. Polyoxometalates electron acceptor-intercalated $In_2O_3$@$SnO_2$ nanofibers for chemiresistive ethanol gas sensors. *Sens. Actuators B* **2024**, *410*, 135728. [CrossRef]
7. Zhang, L.; Wang, T.; Yang, Y.; Wei, M.; Li, F.; Yu, H.; Dong, X. In situ synthesis of polyoxometalate-derived $MoS_2$/phosphomolybdic acid composites for highly sensitive $NO_2$ detection. *J. Alloys Compd.* **2024**, *977*, 173430. [CrossRef]
8. Li, P.; Yang, Y.; Li, F.; Pei, W.; Li, D.; Yu, H.; Dong, X.; Wang, T. Effect of polyoxometalates electron acceptor decoration on $NO_2$ sensing behavior of ZnS microspheres toward rapid and ultrahigh response. *Sens. Actuators B* **2025**, *426*, 137111. [CrossRef]
9. Song, P.; Wang, T. Application of Polyoxometalates in Chemiresistive Gas Sensors: A Review. *ACS Sens.* **2022**, *7*, 3634–3643. [CrossRef]
10. Degler, D.; Weimar, U.; Barsan, N. Current Understanding of the Fundamental Mechanisms of Doped and Loaded Semiconducting Metal-Oxide-Based Gas Sensing Materials. *ACS Sens.* **2019**, *4*, 2228–2249. [CrossRef]
11. Miller, D.R.; Akbar, S.A.; Morris, P.A. Nanoscale metal oxide-based heterojunctions for gas sensing: A review. *Sens. Actuators B* **2014**, *204*, 250–272. [CrossRef]
12. Mizraei, A.; Leonardi, S.G.; Neri, G. Detection of hazardous volatile organic compounds (VOCs) by metal oxide nanostructures-based gas sensors: A review. *Ceram. Int.* **2016**, *42*, 15119–15141. [CrossRef]
13. Imash, A.; Smagulova, G.; Kaidar, B.; Keneshbekova, A.; Kazhdanbekov, R.; Velasco, L.F.; Mansurov, Z. Chemoresistive Gas Sensors Based on Electrospun 1D Nanostructures: Synergizing Morphology and Performance Optimization. *Sensors* **2024**, *24*, 6797. [CrossRef]
14. Meng, F.-J.; Xin, R.-F.; Li, S.-X. Metal Oxide Heterostructures for Improving Gas Sensing Properties: A Review. *Materials* **2023**, *16*, 263. [CrossRef]
15. Singh, A.; Sikarwar, S.; Verma, A.; Yadav, B.C. The recent development of metal oxide heterostructures based gas sensor, their future opportunities and challenges: A review. *Sens. Actuators A* **2021**, *332*, 113127. [CrossRef]
16. Rumyantseva, M.N.; Vladimirova, S.A.; Platonov, V.B.; Chizhov, A.S.; Batuk, M.; Hadermann, J.; Khmelevsky, N.O.; Gaskov, A.M. Sub-ppm $H_2S$ sensing by tubular ZnO-$Co_3O_4$ nanofibers. *Sens. Actuators B* **2020**, *307*, 127624. [CrossRef]
17. Sakai, G.; Matsunaga, N.; Shimanoe, K.; Yamazoe, N. Theory of gas-diffusion controlled sensitivity for thin film semiconductor gas sensor. *Sens. Actuators B* **2001**, *80*, 125–131. [CrossRef]
18. Wang, X.; Wang, Y.; Tian, F.; Liang, H.; Wang, K.; Zhao, X.; Lu, Z.; Jiang, K.; Yang, L.; Lou, X. From the surface reaction control to gas-diffusion control: The synthesis of hierarchical porous $SnO_2$ microspheres and their gas-sensing mechanism. *J. Phys. Chem. C* **2015**, *119*, 15963–15976. [CrossRef]
19. Gong, S.; Liu, J.; Xia, J.; Quan, L.; Liu, H.; Zhou, D. Gas sensing characteristics of $SnO_2$ thin films and analyses of sensor response by the gas diffusion theory. *Mater. Sci. Eng. B* **2009**, *164*, 85–90. [CrossRef]
20. Zakutayev, A.; Paudel, T.R.; Ndione, P.F.; Perkins, J.D.; Lany, S.; Zunger, A.; Ginley, D.S. Cation off-stoichiometry leads to high p-type conductivity and enhanced transparency in $Co_2ZnO_4$ and $Co_2NiO_4$ thin films. *Phys. Rev. B* **2012**, *85*, 085204. [CrossRef]
21. Nemufulwi, M.I.; Swart, H.C.; Shingange, K.; Mnlongo, G.H. $ZnO/ZnFe_2O_4$ heterostructure for conductometric acetone gas sensors. *Sens. Actuators B* **2023**, *377*, 133027. [CrossRef]
22. Greiner, M.T.; Helander, M.G.; Tang, W.-M.; Wang, Z.-B.; Qiu, J.; Lu, Z.-H. Universal energy-level alignment of molecules on metal oxides. *Nat. Mat.* **2021**, *11*, 76–81. [CrossRef] [PubMed]
23. Xu, Q.; Ju, D.; Zhang, Z.; Yuan, S.; Zhang, J.; Xu, H.; Cao, B. Near room-temperature triethylamine sensor constructed with CuO/ZnO P-N heterostructural nanorods directly on flat electrode. *Sens. Actuators B* **2016**, *225*, 16–23. [CrossRef]

24. Shen, Y.-C.; Tung, C.-Y.; Huang, C.-Y.; Lin, Y.-C.; Lin, Y.-G.; Horng, R.H. Study on optoelectronic characteristic of $ZnGa_2O_4$ thin-film phototransistors. *ACS Appl. Electron. Mater.* **2019**, *1*, 783–788. [CrossRef]
25. Lai, T.-Y.; Fang, T.-H.; Hsiao, Y.-J.; Chan, C.-A. Characteristics of Au-doped $SnO_2$–ZnO heteronanostructures for gas sensing applications. *Vacuum* **2019**, *166*, 155–161. [CrossRef]
26. Lang, O.; Pettenkofer, C.; Sánchez-Royo, J.F.; Segura, A.; Klein, A.; Jaegermann, W. Thin film growth and band lineup of $In_2O_3$ on the layered semiconductor InSe. *J. Appl. Phys.* **1999**, *86*, 5687–5691. [CrossRef]
27. Bonch-Bruevich, V.L. Problems of the electron theory of disordered semiconductors. *Sov. Phys. Usp.* **1983**, *26*, 664. [CrossRef]
28. Bârsan, N.; Weimar, U. Conduction model of metal oxide gas sensors. *J. Electroceram.* **2001**, *7*, 143–167. [CrossRef]
29. Barsan, N.; Simion, C.; Heine, T.; Pokhrel, S.; Weimar, U. Modeling of sensing and transduction for p-type semiconducting metal oxide based gas sensors. *J. Electroceram.* **2010**, *25*, 11–19. [CrossRef]
30. Boreskov, G.K. Catalytic activation of dioxygen. In *Catalysis: Science and Technology*; Anderson, J.R., Boudart, M., Eds.; Springer: Berlin/Heidelberg, Germany; New York, NY, USA, 1982; Volume 3, Chapter 2; pp. 39–137. [CrossRef]
31. Idriss, H.; Barteau, M.A. Active sites on oxides: From single crystals to catalysts. *J. Adv. Catal. Sci. Technol.* **2000**, *45*, 261–331. [CrossRef]
32. Jeong, N.C.; Lee, J.S.; Tae, E.L.; Lee, Y.J.; Yoon, K.B. Acidity scale for metal oxides and Sanderson's electronegativities of lanthanide elements. *Angew. Chem. Int. Ed.* **2008**, *47*, 10128–10132. [CrossRef] [PubMed]
33. Vorobyeva, N.A.; Marikutsa, A.V.; Rumyantseva, M.N.; Kozlovskii, V.F.; Filatova, D.G.; Gaskov, A.M. Effect of Ga and in doping on acid centers and oxygen chemisorption on the surface of nanocrystalline ZnO. *Inorg. Mater.* **2016**, *52*, 578–583. [CrossRef]
34. Platonov, V.; Rumyantseva, M.; Khmelevsky, N.; Gaskov, A. Electrospun ZnO/Pd nanofibers: CO sensing and humidity effect. *Sensors* **2020**, *20*, 7333. [CrossRef] [PubMed]
35. Sergent, N.; Epifani, M.; Comini, E.; Faglia, G.; Pagnier, T. Interactions of nanocrystalline tin oxide powder with $NO_2$: A Raman spectroscopic study. *Sens. Actuators B* **2007**, *126*, 1–5. [CrossRef]
36. Prades, J.D.; Cirera, A.; Morante, J.R.; Pruned, J.M.; Ordejón, P. Ab initio study of NOx compounds adsorption on $SnO_2$ surface. *Sens. Actuators B* **2007**, *126*, 62–67. [CrossRef]
37. Leblanc, E.; Perier-Camby, L.; Thomas, G.; Giber, G.; Primet, R.M.; Gelin, P. NOx adsorption onto dehydroxylated or hydroxylated tin oxide surface. Application to $SnO_2$-based gas sensors. *Sens. Actuators B* **2000**, *62*, 67–72. [CrossRef]
38. Wang, J.; Shen, Y.; Li, X.; Xia, Y.; Yang, C. Synergistic effects of UV activation and surface oxygen vacancies on the room temperature $NO_2$ gas sensing performance of ZnO nanowires. *Sens. Actuators B* **2019**, *298*, 126858. [CrossRef]
39. Watanabe, K.; Matsumoto, K.; Ohgaki, T.; Sakaguchi, I.; Ohashi, N.; Hishita, S.; Haneda, H. Development of ZnO-based surface plasmon resonance gas sensor and analysis of UV irradiation effect on $NO_2$ desorption from ZnO thin films. *J. Ceram. Soc. Jpn.* **2010**, *118*, 193–196. [CrossRef]
40. Spencer, M.J.S.; Yarovsky, I. ZnO Nanostructures for Gas Sensing: Interaction of $NO_2$, NO, O, and N with the ZnO(1010) Surface. *J. Phys. Chem. C* **2010**, *114*, 10881–10893. [CrossRef]
41. Breedon, M.; Spencer, M.J.S.; Yarovsky, I. Adsorption of $NO_2$ on Oxygen Deficient ZnO(2110) for Gas Sensing Applications: A DFT Study. *J. Phys. Chem. C* **2010**, *114*, 16603–16610. [CrossRef]
42. Kaur, M.; Shaheera, M.; Pathak, A.; Gadkari, S.C.; Debnath, A.K. Highly sensitive $NO_2$ sensor based on ZnO nanostructured thin film prepared by SILAR technique. *Sens. Actuators B* **2021**, *335*, 129678. [CrossRef]
43. Chen, H.; Qu, Y.; Ding, J.; Fu, H. Adsorption behavior of graphene-like ZnO monolayer with oxygen vacancy defects for $NO_2$: A DFT study. *Superlattices Microstruct.* **2019**, *134*, 106223. [CrossRef]
44. Rodriguez, J.A.; Jirsak, T.; Dvorak, J.; Sambasivan, S.; Fischer, D. Reaction of $NO_2$ with Zn and ZnO: Photoemission, XANES, and Density Functional Studies on the Formation of $NO_3$. *J. Phys. Chem. B* **2000**, *104*, 319–328. [CrossRef]
45. Chizhov, A.; Kutukov, P.; Gulin, A.; Astafiev, A.; Rumyantseva, M. UV-Activated $NO_2$ Gas Sensing by Nanocrystalline ZnO: Mechanistic Insights from Mass Spectrometry Investigations. *Chemosensors* **2022**, *10*, 147. [CrossRef]
46. Vorobyeva, N.; Rumyantseva, M.; Filatova, D.; Konstantinova, E.; Grishina, D.; Abakumov, A.; Turner, S.; Gaskov, A. Nanocrystalline ZnO(Ga): Paramagnetic centers, surface acidity and gas sensor properties. *Sens. Actuators B* **2013**, *182*, 555–564. [CrossRef]